Letter

Ferrorotational domain walls revealed by electric quadrupole second harmonic generation microscopy

Xiaoyu Guo,[1] Rachel Owen,[1] Austin Kaczmarek,[1] Xiaochen Fang,[2] Chandan De,[3,4,5] Youngjun Ahn,[1] Wei Hu,[6,7] Nishkarsh Agarwal,[8] Suk Hyun Sung,[8] Robert Hovden,[8] Sang-Wook Cheong,[2] and Liuyan Zhao[1,*]

[1]*Department of Physics, University of Michigan, Ann Arbor, Michigan 48109, USA*

[2]*Department of Physics and Astronomy, Rutgers Center for Emergent Materials, Rutgers University, Piscataway, New Jersey 08854, USA*

[3]*Center for Artificial Low Dimensional Electronic Systems, Institute for Basic Science (IBS), Pohang 37673, Korea*

[4]*Laboratory of Pohang Emergent Materials, Pohang Accelerator Laboratory, Pohang 37673, Korea*

[5]*2D Crystal Consortium, Materials Research Institute, The Pennsylvania State University, University Park, Pennsylvania 16802, USA*

[6]*School for Environment and Sustainability, University of Michigan, Ann Arbor, Michigan 48109, USA*

[7]*Department of Statistics, University of Michigan, Ann Arbor, Michigan 48109, USA*

[8]*Department of Material Science and Engineering, University of Michigan, Ann Arbor, Michigan 48109, USA*

(Received 17 December 2022; accepted 1 May 2023; published 24 May 2023)

Domain walls are ubiquitous in materials that undergo phase transitions driven by spontaneous symmetry breaking. Domain walls in ferroics and multiferroics have received tremendous attention recently due to their emergent properties distinct from their domain counterparts—for example, their high mobility and controllability, as well as their potential applications in nanoelectronics. However, it is extremely challenging to detect, visualize, and study the ferrorotational (FR) domain walls because the FR order, in contrast to ferromagnetism and ferroelectricity, is invariant under both the spatial-inversion and the time-reversal operations and, thus, hardly couple with conventional experimental probes. Here, a FR candidate $NiTiO_3$ is investigated by ultrasensitive electric quadrupole (EQ) second-harmonic generation rotational anisotropy (SHG RA) to probe the point symmetries of the two degenerate FR domain states, showing their relation by the vertical mirror operations that are broken below the FR critical temperature. We then visualize the real-space FR domains by scanning EQ SHG microscopy, and further, resolve the FR domain walls by revealing a suppressed SHG intensity at the domain walls. By taking local EQ SHG RA measurements, we show the restoration of the mirror symmetry at FR domain walls and prove their unconventional nonpolar nature. Our findings not only provide a comprehensive insight into FR domain walls, but also demonstrate a unique and powerful tool for future studies on domain walls of unconventional ferroics both of which pave the way towards future manipulations and applications of FR domain walls.

DOI: 10.1103/PhysRevB.107.L180102

Domain walls are low-dimensional features that lie between neighboring domains related by broken symmetries through second-order phase transitions in solids. In particular, domain walls in ferroics and multiferroics have attracted tremendous attention and have been intensively studied because of their unique physical properties [1–12] and the applications enabled by their flexible controllability [13–17]. Ferrorotational (FR) order, a ferroic order made of a toroidal arrangement of electric dipoles, distinguishes itself from other ferroic orders by its invariance under both the spatial-inversion and the time-reversal operations. Because of this unique symmetry property, conventional techniques that have been used to investigate different types of ferroic domain walls, such as piezoresponse force microscopy [18], conductive atomic force microscopy [2,19], nitrogen-vacancy center magnetometry [20,21], magneto-optic Kerr effect [22], and electric dipole second-harmonic generation (ED SHG) microscopy [23–25], barely couple to the FR order.

Electric quadrupole (EQ) SHG, in contrast to ED SHG that only survives when spatial inversion is broken, is present in all systems, whereas exhibiting much weaker intensities. Comparing to linear optics and ED SHG, EQ SHG provides more copies of participating vector fields that allow a direct coupling to high-rank multipolar orders (e.g., the FR order). In this Letter, we apply EQ SHG to investigate the FR order of $NiTiO_3$ single crystals. Above $T_c = 1560$ K, $NiTiO_3$ crystallizes in a corundom structure with the space-group $R\bar{3}c$ [point-group $\bar{3}m$, Fig. 1(a)]. The structure possesses a C_3 rotational symmetry along the c axis as well as three mirror planes parallel to the c axis [Fig. 1(b)]. Below T_c, ordering of the metallic ions occurs with Ni^{2+} and Ti^{4+} arranged alternately in a layer-by-layer fashion [26,27]. The resulting two stacking sequences give rise to two domain states A and B [Figs. 1(c) and 1(e)], featuring net structural rotations in opposite directions arising from the different rotational distortions of the oxygen cages [Figs. 1(d) and 1(f)]. These distortions, which break the mirror symmetries and reduce the space group from $R\bar{3}c$ to $R\bar{3}$ (point-group $\bar{3}$), result in a toroidal arrangement of electric dipole moments that lead to FR order.

*Corresponding author: lyzhao@umich.edu

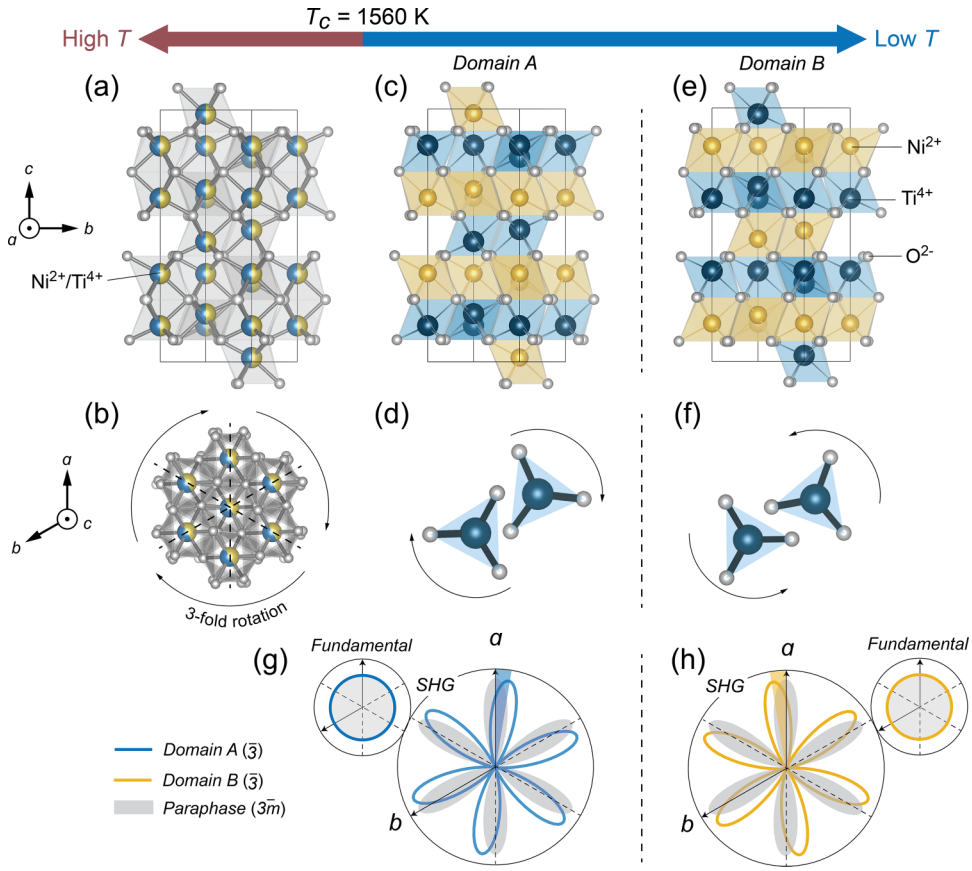

FIG. 1. (a) *a*-axis and (b) *c*-axis views of the $NiTiO_3$ crystal structure above T_c. The threefold rotational symmetry and the three mirrors are indicated by the arrows and the dashed lines. (c) and (e) *a*-axis view of FR domain states *A* and *B* below T_c. (d) and (f) *c*-axis view of two oxygen cages enclosing Ti^{4+} of domains *A* and *B*. Arrows indicate the rotation direction of the oxygen cages. (g) and (h) Simulated polarization-resolved fundamental reflection and the EQ SHG RA in the parallel channel from domain *A*, domain *B*, and from the paraphase.

Due to the centrosymmetric crystal structure, EQ SHG is the lowest rank nonlinear optical process that can couple with FR order. Figures 1(g) and 1(h) show the simulated EQ SHG rotational anisotropy (RA) together with the polarization-resolved fundamental reflection in the parallel channel from FR domains *A* and *B* obtained under normal incidence of light along the *c* axis of the sample. Whereas the polarization-resolved fundamental reflections show identical circular patterns from both domains, the EQ SHG RA patterns exhibit a rotation of the six-lobe patterns in opposite directions between the two FR domains, demonstrating the advantage of EQ SHG in probing FR order and distinguishing the two degenerate FR domain states.

Experimentally, we perform the EQ SHG RA measurements [28] on a normal-cut sample [Fig. 2(a)], whose surface normal is off from the crystal *c* axis by $\theta_1 = 2 \pm 1^\circ$, determined by the group-theory analysis [28] and confirmed by the x-ray diffraction. By performing oblique SHG RA measurements on this sample, we confirm that our SHG signal is primarily from the bulk EQ contribution instead of others, such as bulk magnetic dipole or surface ED [28]. Figures 2(b) and 2(c) show the corrected EQ SHG RA patterns from the two FR domain states under the normal incidence of light [28] with the data (markers) fitted by the simulated functional forms from the point-group $\bar{3}$ (solid lines). Both sets of the EQ SHG RA patterns possess the threefold rotational symmetry but rotate away from the paraphase mirrors in opposite directions by 17°, which is the evidence of the broken mirror symmetry in the FR phase. This 34° rotation angle difference between the EQ SHG RA patterns far exceeds that of the tiny rotational distortions of the crystal structures between the two domains. This rotation of the SHG RA pattern depends on the relative amplitudes between the susceptibility tensor elements of the paraphase and those of the FR phase which are wavelength dependent [28,29]. For $NiTiO_3$, the optical gap (~3 eV, or ~400 nm) [30,31] is close to our SHG wavelength (400 nm) where the optical resonance condition leads to the large rotation of the SHG RA patterns. Such large rotations in the EQ SHG RA patterns have also been observed in other FR materials [29,32,33], corroborating the benefits of EQ SHG RA in distinguishing the degenerate FR domains. Next, in preparation for the domain imaging, we prepared another tilt-cut $NiTiO_3$ sample, whose cut surface is deliberately chosen to be perpendicular to one of the three mirrors of the paraphase with its surface normal off from the crystal *c* axis by $\theta_2 = 34 \pm 6^\circ$ [Fig. 2(d)]. As shown in Figs. 2(e) and 2(f), there is an increase in the SHG signal, the SHG anisotropy, together with a reduction of symmetry in the EQ SHG RA patterns for the tilt-cut sample. The six lobes of the EQ SHG RA patterns with even intensities in the normal-cut sample are reduced to two large and two small lobes in the tilt-cut sample along with the threefold rotational symmetry reduced to twofold. EQ SHG

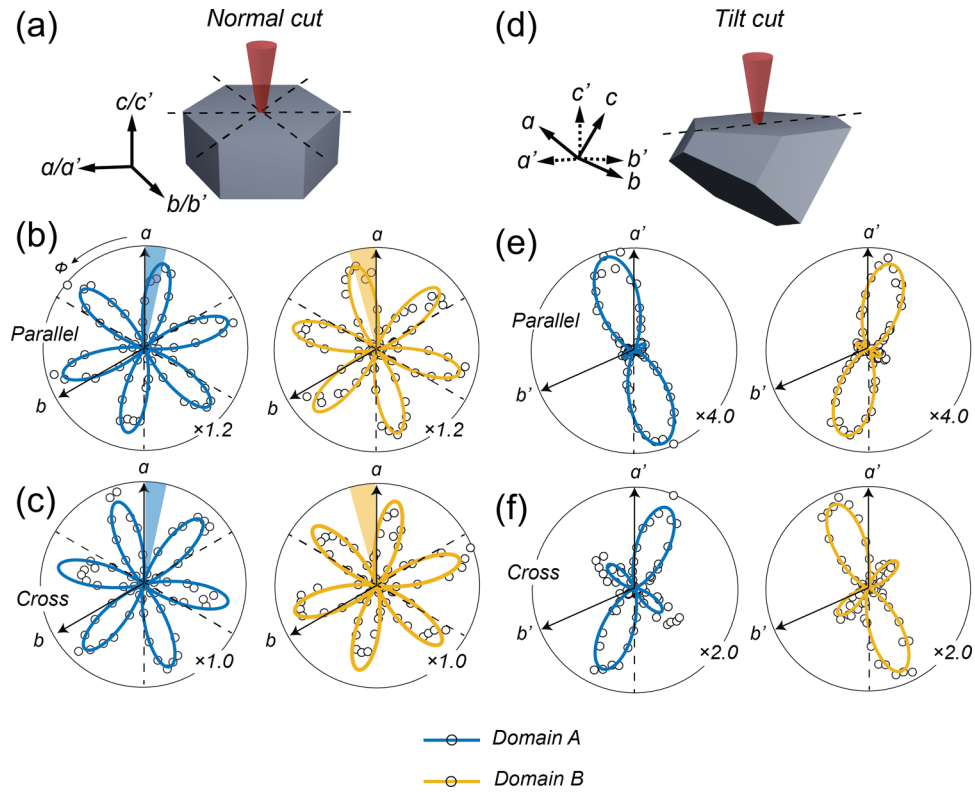

FIG. 2. (a) and (d) Schematics of laser light incident on the normal-cut and the tilt-cut samples. The a' and b' axis are projections of the a and b axes onto the sample cut surface, and the c' axis is the projection of the c axis onto the surface normal. Mirrors of the paraphase are indicated by the dashed lines. (b) and (c) Corrected EQ SHG RA patterns from the normal-cut sample FR domain A (blue) and domain B (yellow) in (b) the parallel and (c) the cross channel. Rotations of the patterns away from the a axis are indicated by the colored shaded areas. (e) and (f) EQ SHG RA patterns from the tilt-cut sample FR domain A (blue) and domain B (yellow) in the (e) parallel and (f) the cross channel. Mirrors of the paraphase are indicated by the dashed lines. Data (markers) are fitted by the functional form from group-theory analysis (solid lines).

RA patterns from the two domains, however, are still related by the vertical mirror operation that is aligned with the a axis of the crystal.

The anisotropy in the tilt-cut sample introduces a large SHG intensity contrast in the parallel channel at the polarization angles $\phi_1 = -17^\circ$ and $\phi_2 = 17^\circ$ [the insets of Figs. 3(a) and 3(b)], allowing us to image the FR domains by the means of scanning EQ SHG microscopy [28]. We first fix the polarization angle to be at $\phi_1 = 17^\circ$ and perform the scanning EQ SHG measurement. The yielded FR domain map is shown in Fig. 3(a). The two degenerate FR domain states are clearly distinguished with a stark contrast and are clearly separated. When the polarization is fixed at $\phi_2 = -17^\circ$, a complimentary FR domain map is constructed and shown in Fig. 3(b) with the signal levels of the two FR domains flipped from Fig. 3(a). Regions highlighted in yellow show exceptionally large SHG signals and correspond to island-shaped NiO defects formed during sample growth [28].

The high-resolution FR domain imaging enables us to perform a series of statistical analyses on the FR domains and domain walls, providing essential yet unprecedented information about the FR order and could be compared with ferroelectric (FE), ferromagnetic (FM), and the ferrotoroidal (FT) orders. First, we calculate the domain populations based on the SHG signal level of each pixel. As is shown in Fig. 3(c), the populations of domains A and B are close to each other, showing no obvious preference to either domain when the FR order is formed. We next investigate the lateral size of the FR domains obtained from the whole scanned region [28] and plot the histogram of the lateral domain size in Fig. 3(d). The domain lateral size mostly lies in the 20–30-μm range, larger than the typical size of the FE domains (1 μm) [2,19,20,34–39], close to that of the FM domains ($\sim$10 μm) [40,41] and smaller than that of the FT domains ($\sim$100 μm) [25,42]. During the sample preparation process, we observe that by quenching the sample across T_c, the domains can shrink by more than 80% of the size of the slow cooling sample domains [28] with an increase in the domain-wall density. The cooling-rate dependence of the domain sizes has also been observed by previous studies [43]. This indicates that the quadrupolar nature of the FR order is distinct from the dipolar ferroic counterparts, such as FM and FE orders whose domain sizes mainly result from the energy competition between long-range (e.g., magnetic dipole-dipole interaction for FM) and short-range (e.g., exchange coupling for FM) interactions [44]. On the contrary, instead of the static energetics, the dominant contributor to the formation of the FR domains and their size could be the nonequilibrium dynamics as well as the formation of topological defects during the cooling process of the sample growth [45,46].

Besides the FR domains, we can also visualize the boundaries between the two FR domains, i.e., the domain walls.

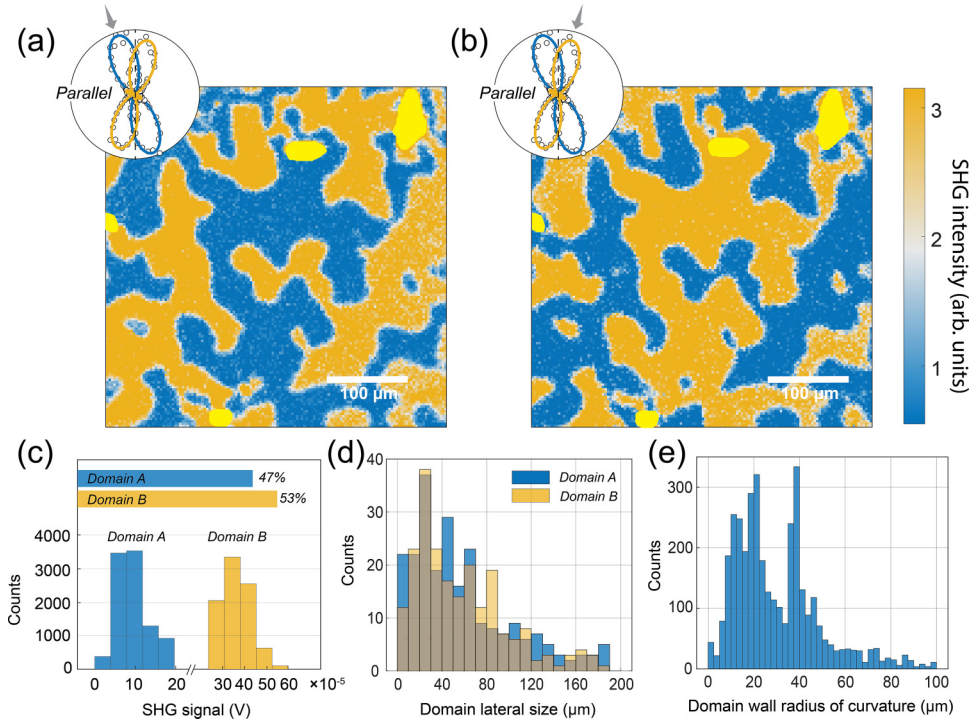

FIG. 3. (a) and (b) EQ SHG scanning of the FR domains at the polarizations indicated by the corresponding insets. Regions with exceptionally large SHG signals are highlighted by the yellow color. (c)–(e) Histogram of (c) the population of FR domains, (d) the domain lateral size, and (e) the radius of curvature along the domain walls.

Figure 3(e) plots the histogram of the radius of curvature extracted from each point along the domain wall [28]. Two peak frequencies appear at 10–22.5 and 35–40 μm, which are comparable to the characteristic lateral domain sizes (20–30 μm). This is consistent with the meandering of the domain wall shown in Figs. 3(a) and 3(b) and is in stark contrast to the straight-wall morphology that is ubiquitous in strain-induced ferroelectric and ferroelastic materials [2,39,47]. However, in FT [25,42], FM [40,41], and many of the improper FE materials [4,38,48], the domain walls also show curving profiles, similar to the case of FR domains in $NiTiO_3$. We infer from this observation that the domain walls tend to be curved when the order parameter is parallel to the out-of-plane rotational axis (i.e., c axis in $NiTiO_3$) and, hence, does not break any rotational symmetry. This is because such types of order parameters have zero component projected onto the in-plane domain walls and, therefore, are relatively insensitive to the curving of them.

Remarkably, scanning EQ SHG and local EQ SHG RA measurements can be applied to selectively image the domain walls and probe their symmetries. As shown in Fig. 4(a) within the selected region shown in the lower inset, by choosing the polarization in the cross channel along the a axis where both FR domains yield the same SHG signal level [Fig. 4(a) upper inset], the EQ SHG scanning image shows a clear suppression of SHG intensity at the domain walls as compared to the domains on both sides. The average SHG signal is calculated along the domain wall [green contour in Fig. 4(b)] as well as along the contours that are further away from it [28]. The plot of the average SHG intensity as a function of the distance to the domain wall is shown in Fig. 4(c). The valley of the plot corresponds to the domain wall as expected from the scanning EQ SHG image in Fig. 4(a). The drop of the signal at the boundaries is the signature of mirror symmetry along the incident light polarization, which forbids any SHG signal in the cross channel, in contrast to the absence of mirrors inside FR domains. We note that similar suppression of the SHG signal at the domain boundaries was also observed in polycrystalline MoS_2 [49,50] due to the destructive interference between the SHG light from adjacent domains [23,25,51]. We have ruled out the possibility of destructive interference in our experiment and confirmed that the suppression of SHG intensity results from the restoration of mirror symmetry at the domain walls [28]. At the same time, we also performed SHG imaging in the parallel channel with the polarization aligned with the a axis where no SHG intensity contrast at the domain walls is observed [28]. This confirms that the suppressed SHG in Fig. 4 is governed by the $\bar{3}m$ symmetry. We note that a recent publication reports enhanced SHG at the domain walls [52]. This difference is likely due to the different sample preparation methods that are known to result in different domain morphology [43] and, hence, perhaps different domain-wall characteristics. Besides, the SHG is collected without polarization analysis in Ref. [52]. This geometry always has finite SHG intensity at the domain walls even under $\bar{3}m$, whose relative strength to that inside domains depends on the incident wavelength that differs between Ref. [52] and this Letter [28]. The uniform drop of the signal along the domain wall negates its polar nature since polar domain walls break the spatial-inversion symmetry and, therefore, are expected to show much stronger SHG from the leading order

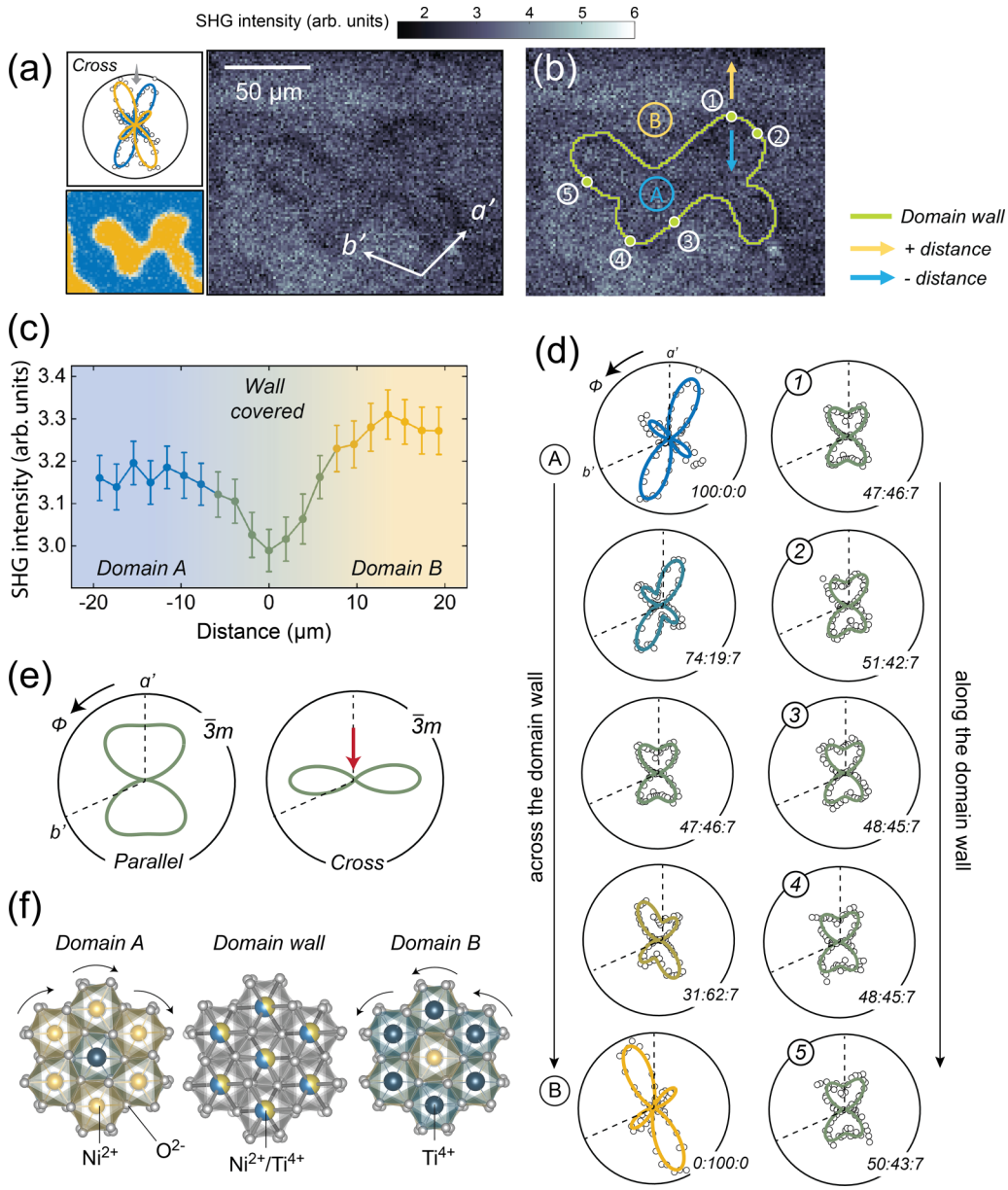

FIG. 4. (a) EQ SHG scanning image of the domain walls in the cross channel at the polarization indicated by the arrow in the upper inset. The lower inset shows the same region of interest extracted from Fig. 3(a). (b) Same as (a), where domains *A* and *B* are labeled. The green contour indicates the domain wall based on which (c) is constructed. The blue/yellow arrows and numbers indicate where EQ SHG RA is measured and plotted in (d). (c) Averaged EQ SHG intensity as a function of distance to the domain wall. (d) EQ SHG RA patterns in the cross channel measured across and along the domain wall. Numbers at the bottom right of the plots indicate the ratio of contributions from domains *A*, *B*, and the domain walls. (e) Simulated EQ SHG RA from a tilt-cut sample based on $\bar{3}m$. The red arrow indicates the polarization parallel to the mirror. (f) *c*-axis view of the crystal structures of domains *A*, *B*, and the domain wall. Arrows indicate the rotation direction of the oxygen cages.

ED contribution [7]. The signal drop at the domain wall of our $NiTiO_3$ is $7.0 \pm 1.5\%$ compared to the average signal level of the two FR domains, yielding an estimated domain-wall width to be 0.76 ± 0.20 μm [28]. This estimated domain-wall width lies within the range of the previously reported values by scanning-tunneling electron microscopy, ranging from several nanometers to several micrometers [53] and is also confirmed by our scanning electron microscopy (SEM) measurements [28]. Depending on the relative orientation of the domain walls to the surface normal, we may have overestimated the domain-wall width by probing its tilt-cut cross section. Therefore, our measured wall width is an upper bound of the actual value.

To further characterize the domain walls, we perform a series of EQ SHG RA measurements across and along the domain wall. The left column of Fig. 4(d) shows the EQ SHG RA measured across the domain wall along the blue and the yellow arrows shown in Fig. 4(b). From domain *A* to domain *B*, there is a continuous evolution of the EQ SHG RA patterns and between the domains, the EQ SHG RA shows intermediate patterns, which result from the superposition of the contributions from the two FR domains and the domain

wall. The right column of Fig. 4(d) shows the EQ SHG RA patterns measured along the domain wall at the positions labeled by the numbers shown in Fig. 4(b). All EQ SHG RA patterns measured at different positions on the domain wall show almost identical bow-tie shapes. This confirms the nonpolar nature of the domain wall and shows stark contrast to the polar domain walls of ferroelastic materials, such as $CaTiO_3$ [7] where the shapes of the SHG RA patterns are locked to the curving directions of domain walls.

Having established the presence of the mirror symmetry at the domain walls, we here propose that the domain walls retain the crystal structure of the paraphase and preserve the mirror symmetries, in contrast to the FR domains where the ordering of Ni^{2+} and Ti^{4+} takes place below T_c [Fig. 4(f)]. Similar situations are also present in ferroelectricity, such as $BiFeO_3$ where at the domain boundaries, it is more energetically favorable for the oxygen octahedra to remain unchanged [54]. To confirm this, Fig. 4(e) shows the simulated EQ SHG RA patterns from a tilt-cut sample based on the $\bar{3}m$ point group of the paraphase using the susceptibility tensor elements extracted from the fitting results of the FR domain data [Figs. 2(e) and 2(f)]. The red arrow indicates that indeed, SHG radiation is suppressed at the polarization aligned with the mirror in the cross channel, consistent with the intensity suppression at domain walls in Fig. 4(a). We then construct the superposition of the EQ SHG RA patterns from both the FR domains and the domain walls, which is used to fit the EQ SHG RA data in Fig. 4(d) (solid curves). The weight of the contributions from domains *A*, *B*, and walls are displayed at the bottom right corner of each polar plot.

To summarize, the spatial distribution and symmetries of FR domains in $NiTiO_3$ are carefully investigated by ultrasensitive EQ SHG techniques. More importantly, these EQ SHG techniques further enable us to selectively resolve the domain walls and probe their symmetries, despite the presence of spatial-inversion symmetry. We observe the meandering feature of the FR domain walls and confirm the presence of mirrors at the domain walls as well as their nonpolar natures. The high-resolution FR domain and domain-wall maps enabled by the EQ SHG techniques pave the way for the future study on the interactions between the FR order and other orders coexisting in a system. It has been suggested that in many type-II multiferroics, the FR order is a prerequisite for subsequent noncentrosymmetric magnetic orders, which are the necessary ingredients for type-II multiferroicity [55–57]. For $NiTiO_3$, it has been reported that an antiferromagnetic (AFM) order forms below $T_{AFM} = 23$ K [58–60]. It would be insightful to explore how the AFM order is established upon the existing FR orders, and how the AFM domains distribute in the presence of FR domains and domain walls.

L.Z. acknowledges support by NSF CAREER Grant No. DMR-174774, AFOSR YIP Grant No. FA9550-21-1-0065, and the Alfred P. Sloan Foundation. The work at Rutgers University was supported by the DOE under Grant No. DOE: DE-FG02-07ER46382 and the W.M. Keck Foundation. R.H. acknowledges support from ARO Grant No. W911NF-22-1-0056. X.G., S.-W.C., and L.Z. conceived the experiment. X.G. performed the experiment. X.G. and R.O. analyzed the data. X.G. and A.K. constructed the SHG setup. C.D. grew the crystal under the guidance of S.-W.C. X.F. prepared the sample surface for the SHG measurements. W.H. analyzed the domain boundary data. N.A., S.H.S, and R.H. performed the SEM measurements. X.G., Y.A. and L.Z. wrote the Letter.

[1] L. Goncalves-Ferreira, S. A. T. Redfern, E. Artacho, and E. K. H. Salje, Ferrielectric Twin Walls in $CaTiO_3$, Phys. Rev. Lett. **101**, 097602 (2008).

[2] J. Seidel, L. W. Martin, Q. He, Q. Zhan, Y. H. Chu, A. Rother, M. E. Hawkridge, P. Maksymovych, P. Yu, M. Gajek *et al.*, Conduction at domain walls in oxide multiferroics, Nature Mater. **8**, 229 (2009).

[3] J. Guyonnet, I. Gaponenko, S. Gariglio, and P. Paruch, Conduction at domain walls in insulating $Pb(Zr_{0.2}Ti_{0.8})O_3$ thin films, Adv. Mater. **23**, 5377 (2011).

[4] Y. N. Geng, N. Lee, Y. J. Choi, S. W. Cheong, and W. D. Wu, Collective magnetism at multiferroic vortex domain walls, Nano Lett. **12**, 6055 (2012).

[5] J. F. Scott, E. K. H. Salje, and M. A. Carpenter, Domain Wall Damping and Elastic Softening in $SrTiO_3$: Evidence for Polar Twin Walls, Phys. Rev. Lett. **109**, 187601 (2012).

[6] T. Sluka, A. K. Tagantsev, P. Bednyakov, and N. Setter, Free-electron gas at charged domain walls in insulating $BaTiO_3$, Nat. Commun. **4**, 1808 (2013).

[7] H. Yokota, H. Usami, R. Haumont, P. Hicher, J. Kaneshiro, E. K. H. Salje, and Y. Uesu, Direct evidence of polar nature of ferroelastic twin boundaries in $CaTiO_3$ obtained by second harmonic generation microscope, Phys. Rev. B **89**, 144109 (2014).

[8] X. K. Wei, A. K. Tagantsev, A. Kvasov, K. Roleder, C. L. Jia, and N. Setter, Ferroelectric translational antiphase boundaries in nonpolar materials, Nat. Commun. **5**, 3031 (2014).

[9] T. Rojac, A. Bencan, G. Drazic, N. Sakamoto, H. Ursic, B. Jancar, G. Tavcar, M. Makarovic, J. Walker, B. Malic *et al.*, Domain-wall conduction in ferroelectric $BiFeO_3$ controlled by accumulation of charged defects, Nature Mater. **16**, 322 (2017).

[10] J. Ma, J. Ma, Q. H. Zhang, R. C. Peng, J. Wang, C. Liu, M. Wang, N. Li, M. F. Chen, X. X. Cheng *et al.*, Controllable conductive readout in self-assembled, topologically confined ferroelectric domain walls, Nat. Nanotechnol. **13**, 972 (2018).

[11] H. Yokota, S. Matsumoto, E. K. H. Salje, and Y. Uesu, Symmetry and three-dimensional anisotropy of polar domain boundaries observed in ferroelastic $LaAlO_3$ in the complete absence of ferroelectric instability, Phys. Rev. B **98**, 104105 (2018).

[12] H. Yokota, S. Matsumoto, E. K. H. Salje, and Y. Uesu, Polar nature of domain boundaries in purely ferroelastic $Pb_3(PO_4)_2$ investigated by second harmonic generation microscopy, Phys. Rev. B **100**, 024101 (2019).

[13] J. R. Whyte and J. M. Gregg, A diode for ferroelectric domain-wall motion, Nat. Commun. **6**, 7361 (2015).

[14] W. D. Yang, G. Tian, H. Fan, Y. Zhao, H. Y. Chen, L. Y. Zhang, Y. D. Wang, Z. Fan, Z. P. Hou, D. Y. Chen *et al.*, Nonvolatile ferroelectric-domain-wall memory embedded in a complex topological domain structure, Adv. Mater. **34**, 2107711 (2022).

[15] H. W. Shin, J. H. Son, and J. Y. Son, Current change due to artificial patterning of the number of ferroelectric domain walls and nonvolatile memory characteristics, Appl. Phys. Lett. **119**, 122901 (2021).

[16] P. Sharma, Q. Zhang, D. Sando, C. H. Lei, Y. Y. Liu, J. Y. Li, V. Nagarajan, and J. Seidel, Nonvolatile ferroelectric domain wall memory, Sci. Adv. **3**, e1700512 (2017).

[17] G. Sanchez-Santolino, J. Tornos, D. Hernandez-Martin, J. I. Beltran, C. Munuera, M. Cabero, A. Perez-Munoz, J. Ricote, F. Mompean, M. Garcia-Hernandez *et al.*, Resonant electron tunnelling assisted by charged domain walls in multiferroic tunnel junctions, Nat. Nanotechnol. **12**, 655 (2017).

[18] A. Gruverman, M. Alexe, and D. Meier, Piezoresponse force microscopy and nanoferroic phenomena, Nat. Commun. **10**, 1661 (2019).

[19] D. Meier, J. Seidel, A. Cano, K. Delaney, Y. Kumagai, M. Mostovoy, N. A. Spaldin, R. Ramesh, and M. Fiebig, Anisotropic conductance at improper ferroelectric domain walls, Nature Mater. **11**, 284 (2012).

[20] I. Gross, W. Akhtar, V. Garcia, L. J. Martinez, S. Chouaieb, K. Garcia, C. Carretero, A. Barthelemy, P. Appel, P. Maletinsky *et al.*, Real-space imaging of non-collinear antiferromagnetic order with a single-spin magnetometer, Nature (London) **549**, 252 (2017).

[21] F. Casola, T. van der Sar, and A. Yacoby, Probing condensed matter physics with magnetometry based on nitrogen-vacancy centres in diamond, Nat. Rev. Mater. **3**, 17088 (2018).

[22] Z. C. Luo, A. Hrabec, T. P. Dao, G. Sala, S. Finizio, J. X. Feng, S. Mayr, J. Raabe, P. Gambardella, and L. J. Heyderman, Current-driven magnetic domain-wall logic, Nature (London) **579**, 214 (2020).

[23] M. Trassin, G. De Luca, S. Manz, and M. Fiebig, Probing ferroelectric domain engineering in $BiFeO_3$ thin films by second harmonic generation, Adv. Mater. **27**, 4871 (2015).

[24] D. Meier, M. Maringer, T. Lottermoser, P. Becker, L. Bohaty, and M. Fiebig, Observation and Coupling of Domains in a Spin-Spiral Multiferroic, Phys. Rev. Lett. **102**, 107202 (2009).

[25] B. B. Van Aken, J. P. Rivera, H. Schmid, and M. Fiebig, Observation of ferrotoroidic domains, Nature (London) **449**, 702 (2007).

[26] H. Boysen, F. Frey, M. Lerch, and T. Vogt, A neutron powder investigation of the high-temperature phase-transition in $NiTiO_3$, Z. Kristallogr.-Cryst. Mater. **210**, 328 (1995).

[27] M. Lerch, H. Boysen, R. Neder, F. Frey, and W. Laqua, Neutron-scattering investigation of the high-temperature phase-transition in $NiTiO_3$, J. Phys. Chem. Solids **53**, 1153 (1992).

[28] See Supplemental Material at http://link.aps.org/supplemental/10.1103/PhysRevB.107.L180102 for additional information on material preparation and experimental methods, group-theory analysis of EQ SHG RA, oblique SHG RA measurement on the unannealed normal-cut $NiTiO_3$, normal incidence EQ SHG RA of the unannealed normal-cut $NiTiO_3$, SHG signal contrast between the normal-cut and the tilt-cut samples, FR domain maps color-scale determination, exceptionally large SHG signals from NiO defects, EQ SHG scanning microscopy of the unannealed normal-cut $NiTiO_3$, radius of curvature along the domain walls of the annealed and quenched tilt-cut $NiTiO_3$, discussion of destructive interference at the domain boundary, estimation of the domain-wall width, and SHG domain imaging in the parallel channel and symmetry-enforced SHG suppression at the domain walls.

[29] W. C. Jin, E. Drueke, S. W. Li, A. Admasu, R. Owen, M. Day, K. Sun, S. W. Cheong, and L. Y. Zhao, Observation of a ferro-rotational order coupled with second-order nonlinear optical fields, Nat. Phys. **16**, 42 (2020).

[30] M. W. Li, J. P. Yuan, X. M. Gao, E. Q. Liang, and C. Y. Wang, Structure and optical absorption properties of $NiTiO_3$ nanocrystallites, Appl. Phys. A. Mater. Sci. Process **122**, 725 (2016).

[31] Y. J. Lin, Y. H. Chang, W. D. Yang, and B. S. Tsai, Synthesis and characterization of ilmenite $NiTiO_3$ and $CoTiO_3$ prepared by a modified Pechini method, J. Non-Cryst. Solids **352**, 789 (2006).

[32] X. P. Luo, D. Obeysekera, C. Won, S. H. Sung, N. Schnitzer, R. Hovden, S. W. Cheong, J. J. Yang, K. Sun, and L. Y. Zhao, Ultrafast Modulations and Detection of a Ferro-Rotational Charge Density Wave using Time-Resolved Electric Quadrupole Second Harmonic Generation, Phys. Rev. Lett. **127**, 126401 (2021).

[33] R. Owen, E. Drueke, C. Albunio, A. Kaczmarek, W. C. Jin, D. Obeysekera, S. W. Cheong, J. J. Yang, S. Cundiff, and L. Y. Zhao, Second-order nonlinear optical and linear ultraviolet-visible absorption properties of the type-II multiferroic candidates $RbFe(AO_4)_2$ (A = Mo, Se, S), Phys. Rev. B **103**, 054104 (2021).

[34] A. Schilling, R. M. Bowman, G. Catalan, J. F. Scott, and J. M. Gregg, Morphological control of polar orientation in single-crystal ferroelectric nanowires, Nano Lett. **7**, 3787 (2007).

[35] C. J. M. Daumont, D. Mannix, S. Venkatesan, G. Catalan, D. Rubi, B. J. Kooi, J. T. M. De Hosson, and B. Noheda, Epitaxial $TbMnO_3$ thin films on $SrTiO_3$ substrates: A structural study, J. Phys.: Condens. Matter. **21**, 182001 (2009).

[36] C. C. Neacsu, B. B. van Aken, M. Fiebig, and M. B. Raschke, Second-harmonic near-field imaging of ferroelectric domain structure of $YMnO_3$, Phys. Rev. B **79**, 100107(R) (2009).

[37] A. Schilling, D. Byrne, G. Catalan, K. G. Webber, Y. A. Genenko, G. S. Wu, J. F. Scott, and J. M. Gregg, Domains in ferroelectric nanodots, Nano Lett. **9**, 3359 (2009).

[38] T. Choi, Y. Horibe, H. T. Yi, Y. J. Choi, W. D. Wu, and S. W. Cheong, Insulating interlocked ferroelectric and structural antiphase domain walls in multiferroic $YMnO_3$, Nature Mater. **9**, 253 (2010).

[39] J. Seidel, P. Maksymovych, Y. Batra, A. Katan, S. Y. Yang, Q. He, A. P. Baddorf, S. V. Kalinin, C. H. Yang, J. C. Yang *et al.*, Domain Wall Conductivity in La-doped $BiFeO_3$, Phys. Rev. Lett. **105**, 197603 (2010).

[40] W. Kuch, in *Magnetic Microscopy of Nanostructures*, edited by H. Hopster and H. P. Oepen (Springer, Berlin/Heidelberg, 2005), p. 1.

[41] W. Szmaja, Recent developments in the imaging of magnetic domains, Adv. Imaging. Electron. Phys. **141**, 175 (2006).

[42] A. S. Zimmermann, D. Meier, and M. Fiebig, Ferroic nature of magnetic toroidal order, Nat. Commun. **5**, 4796 (2014).

[43] T. Hayashida, Y. Uemura, K. Kimura, S. Matsuoka, M. Hagihala, S. Hirose, H. Morioka, T. Hasegawa, and T. Kimura, Phase transition and domain formation in ferroaxial crystals, Phys. Rev. Mater. **5**, 124409 (2021).

[44] D. M. Evans, V. Garcia, D. Meier, and M. Bibes, Domains and domain walls in multiferroics, Physica. Sci. Rev. **5**, 20190067 (2020).

[45] H. Okino, J. Sakamoto, and T. Yamamoto, Cooling-rate-dependent domain structures of $Pb(Mg_{1/3}Nb_{2/3})O_3-PbTiO_3$ single crystals observed by contact resonance piezoresponse force microscopy, Jpn. J. Appl. Phys. **43**, 6808 (2004).

[46] S. C. Chae, N. Lee, Y. Horibe, M. Tanimura, S. Mori, B. Gao, S. Carr, and S. W. Cheong, Direct Observation of the Proliferation of Ferroelectric Loop Domains and Vortex-Antivortex Pairs, Phys. Rev. Lett. **108**, 167603 (2012).

[47] Y. Uesu, S. Kurimura, and Y. Yamamoto, Optical second harmonic images of 90° domain structure in $BaTiO_3$ and periodically inverted antiparallel domains in $LiTaO_3$, Appl. Phys. Lett. **66**, 2165 (1995).

[48] T. Jungk, A. Hoffmann, M. Fiebig, and E. Soergel, Electrostatic topology of ferroelectric domains in $YMnO_3$, Appl. Phys. Lett. **97**, 012904 (2010).

[49] J. X. Cheng, T. Jiang, Q. Q. Ji, Y. Zhang, Z. M. Li, Y. W. Shan, Y. F. Zhang, X. G. Gong, W. T. Liu, and S. W. Wu, Kinetic nature of grain boundary formation in as-grown MoS_2 monolayers, Adv. Mater. **27**, 4069 (2015).

[50] X. B. Yin, Z. L. Ye, D. A. Chenet, Y. Ye, K. O'Brien, J. C. Hone, and X. Zhang, Edge nonlinear optics on a MoS_2 atomic monolayer, Science **344**, 488 (2014).

[51] N. Leo, A. Bergman, A. Cano, N. Poudel, B. Lorenz, M. Fiebig, and D. Meier, Polarization control at spin-driven ferroelectric domain walls, Nat. Commun. **6**, 6661 (2015).

[52] H. Yokota, T. Hayashida, D. Kitahara, and T. Kimura, Three-dimensional imaging of ferroaxial domains using circularly polarized second harmonic generation microscopy, npj Quantum Mater. **7**, 106 (2022).

[53] T. Hayashida, Y. Uemura, K. Kimura, S. Matsuoka, D. Morikawa, S. Hirose, K. Tsuda, T. Hasegawa, and T. Kimura, Visualization of ferroaxial domains in an order-disorder type ferroaxial crystal, Nat. Commun. **11**, 4582 (2020).

[54] A. Lubk, S. Gemming, and N. A. Spaldin, First-principles study of ferroelectric domain walls in multiferroic bismuth ferrite, Phys. Rev. B **80**, 104110 (2009).

[55] R. D. Johnson, S. Nair, L. C. Chapon, A. Bombardi, C. Vecchini, D. Prabhakaran, A. T. Boothroyd, and P. G. Radaelli, $Cu_3Nb_2O_8$: A Multiferroic with Chiral Coupling to the Crystal Structure., Phys. Rev. Lett. **107**, 137205 (2011).

[56] A. J. Hearmon, F. Fabrizi, L. C. Chapon, R. D. Johnson, D. Prabhakaran, S. V. Streltsov, P. J. Brown, and P. G. Radaelli, Electric Field Control of the Magnetic Chiralities in Ferroaxial Multiferroic $RbFe(MoO_4)_2$, Phys. Rev. Lett. **108**, 237201 (2012).

[57] R. D. Johnson, L. C. Chapon, D. D. Khalyavin, P. Manuel, P. G. Radaelli, and C. Martin, Giant Improper Ferroelectricity in the Ferroaxial Magnet $CaMn_7O_{12}$, Phys. Rev. Lett. **108**, 067201 (2012).

[58] G. Shirane, S. J. Pickart, and Y. Ishikawa, Neutron diffraction study of antiferromagnetic $MnTiO_3$ and $NiTiO_3$, J. Phys. Soc. Jpn. **14**, 1352 (1959).

[59] A. Ito, H. Kawano, H. Yoshizawa, and K. Motoya, Magnetic-properties and phase-diagram of $Ni_xMn_{1-X}TiO_3$, J. Magn. Magn. Mater. **104**, 1637 (1992).

[60] Y. Yamaguchi, T. Nakano, Y. Nozue, and T. Kimura, Magnetoelectric Effect in an XY-like Spin Glass System $Ni_xMn_{1-x}TiO_3$, Phys. Rev. Lett. **108**, 057203 (2012).